Implementation of a novel nonthermal plasma air cleaner in a plant factory

Masaaki Okubo
Department of Mechanical Engineering, Osaka Prefecture University
1-1 Gakuen-cho, Naka-ku, Sakai 599-8531, Japan
email: mokubo@mokubo.com

*The final publication of this book chapter is
M. Okubo, Implementation of a Novel Nonthermal Plasma Air Cleaner in a Plant Factory, Nonthermal Processing in Agri-Food-Bio Sciences: Sustainability and Future Goals, Anet Režek Jambrak, Editor, Springer, pp. 385-408, Sep. 2022.

Keywords: ion cluster, indoor air cleaning, nonthermal plasma, sterilization, bacteria, fungi, plant factory, HEPA, iceplant

1. Introduction

Lettuce and iceplant are increasingly being cultivated and harvested in plant factories. However, the cultivated items and their uses, such as their consumption as general raw foods, processed foods, and medical products, are diversifying, and the plant factory specifications for each of these uses are very different. For example, when we produce high-value-added plants that suppress the number of viable bacteria and can be eaten without being washed or used as raw materials for cosmetics and medical treatments, the plant cultivation environment should be optimized and cleaned. Therefore, artificially-lit plant factories are often used, as they have closed environments. Such plant factories form the focus of this study. In order to clean the environment of the plant factory, high-efficiency particulate air (HEPA) filters are generally used. However, higher capital and running costs are required because of the large pressure drop and the higher cost of the filter.

We focus on an artificially-lit plant factory and review the application of an ion emission-type nonthermal plasma air cleaner as a low-cost technology for realizing sterilization in the factory [1,2]. Furthermore, we develop a numerical prediction technology for ion concentration and experimentally examine the sterilization ability of the cleaner. Finally, we report on the validity of the nonthermal plasma air cleaner.

2. Clean-up technologies for the environment of an artificially-lit plant factory

2.1 Conventional technology with HEPA filter air cleaner

In an artificially-lit factory [1,2], plants can be produced via pesticide-free cultivation. These plants can be eaten without being washed, have a low viable cell count, can be stored for a long duration, and appeal to consumers as they can be safely consumed. When cultivated in this manner, the plants produced do not have to be cleaned at the time of processing, which is an advantage. In order to realize pesticide-free cultivation, a clean environment is required, and cleanliness achieved through hygiene management, such as in food factories, is important. Plant factories using artificial light have a lower risk of dust, germs, and pest invasion than solar-powered plant factories.

In general, dust, germs, and pests enter and exit artificially-lit plant factories through the entry and exit points for workers and items; further, there is a high possibility that the dust, germs, and pests are brought in by the workers and items. Therefore, installing an air curtain at

the entrance and an air cleaning system in a cleanroom can effectively prevent the entry of dust, germs, and pests. After minimizing the number of entrances and exits, a front room, air shower, airlock room equipment, and handwashing station provide effective protection when workers enter and leave the room. Furthermore, the wearing of a clean suit, sterilization of carried-in items, and possible further measures are also important. A certain degree of cleanliness should be ensured in the cultivation room; however, no clear standards that should be followed exist, and cleanliness is managed according to the cultivated item and its use.

The cleanliness of a cleanroom in a plant factory varies from ISO class 6 to 8 depending on the facility, but in several cases, it is ISO class 8. Cleanliness in these facilities is obtained through general hygiene control, such as the number of airborne particles, the concentration of CO_2, and temperature control. Since the generation of suspended particles that will affect the cleanliness is expected to differ from case to case, criteria for determining whether a cultivation room has been efficiently cleaned may be obtained by understanding the relationship between actual cleanliness and the number of viable bacteria. An air cleaning system using a HEPA filter is generally used to clean a cultivation room. A HEPA filter is used to remove dust and fumes from the air to create clean air. This is the primary filter used in a cleanroom for manufacturing electronic components. Based on the Japan Industrial Standard (JIS), JIS Z 8122 stipulates that a HEPA air filter should have a minimum particle collection rate of 99.97% and a maximum initial pressure loss of 245 Pa for 0.3 μm particles with a rated air volume. The higher the performance of the filter, the larger the ventilation pressure loss, and the larger the fan power required.

2.2 New technology with nonthermal plasma air cleaner

In this study, we aim to replace a HEPA-filtered air cleaner with a low pressure-loss nonthermal plasma air cleaner. An ion emission-type plasma air cleaner is a device that generates positive and negative ions via plasma discharge and releases them into the air. **Fig. 1** shows the sterilization process [1,3]. After adhering to the surface of an airborne bacterium, the released positive and negative ions are transformed into OH radicals with extremely high oxidizing power. Then, by the OH radicals' instant extraction of hydrogen atoms from the protein on the cell wall of the floating bacterium, the protein is decomposed, and the floating bacterium whose cell wall has been destroyed ceases to pose any hazard. The OH radical binds to the hydrogen atom extracted from the protein and returns to the air as water. Plasma air cleaners can suppress the action of airborne bacteria, eradicate airborne mold bacteria, and suppress the growth of adherent mold bacteria. The decomposition and removal of adherent odors are also realized by such a mechanism.

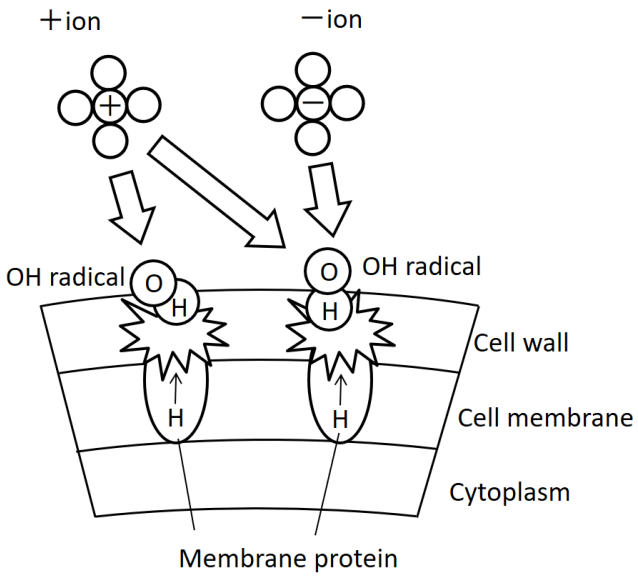

Fig. 1 sterilization process of airborne bacteria with ions [3].

3. Design and simulation of nonthermal plasma air cleaner

3.1 Generation of positive and negative ions in nonthermal plasma air cleaner

We focus on the plasma air cleaner design, which was difficult to realize [4]. We intend to build an analysis model for the numerical simulation of the plasma reactor part (ion generation device), which generates plasma in the plasma air cleaner. To develop a plasma reactor part similar to the actual ion generation device, we aim to build an analysis model by adopting an axisymmetric two-dimensional numerical simulation. To this end, among the various plasma parameters, the following are numerically predicted: electron temperature, electron number density, positive ion ($H_3O^+(H_2O)_n$ [n = 0–5]), molecular number density, and negative ion ($O_2^-(H_2O)_n$ [n = 0–5]). Numerical simulations are conducted on the ion cluster formation of such ion generation devices. The behavior of streamer evolution and cluster formations are simulated, and we demonstrate that the clustering progresses toward $H_3O^+(H_2O)_4$ and $O_2^-(H_2O)_4$ when the chemical species of $H_3O^+(H_2O)_n$ and $O_2^-(H_2O)_n$ (n = 0–5) are considered, as shown in **Fig. 2**. The ion number densities measured in the study are smaller than those calculated considering the known differences between the numerical model and the experimental apparatus (in particular, the difference due to the loss of ions in the path of the chamber). The evaluation of the lifetime and the diffusion coefficients of the ion clusters can be predicted.

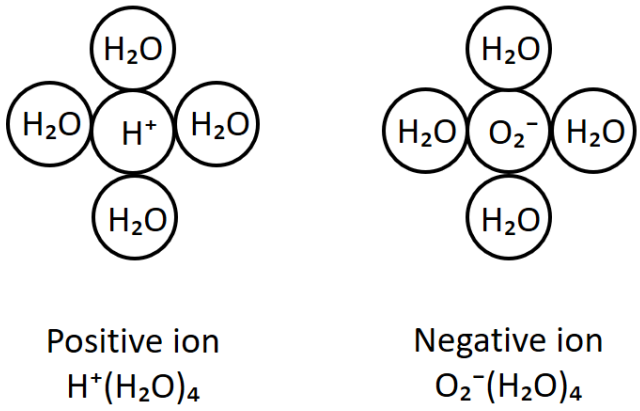

Fig. 2 Dominant ion clusters generated in the plasma air cleaner.

3.2 Numerical prediction of formation of ion clusters

3.2.1 Nonthermal plasma reactor

In the present study, the nonthermal plasma (NTP) reactor or ion generation device inside a plasma electric air cleaner that uses a pulsed corona discharge is analyzed. When a pulsed high voltage is applied to a pair of electrodes at atmospheric pressure, both negative and positive ions are induced as well as high-speed electrons and radicals. These ions are useful for cleaning out hazardous gases, e.g., odorous gases such as ammonia, from the atmosphere. A numerical simulation of the induced atmospheric plasma is carried out for such air cleaners or ion generation devices. It is noted that the induced negative/positive ions may improve human health and decompose allergens.

3.2.2 Numerical model

As shown in **Fig. 3**, the analytical model consists of discharge and ground electrodes based on a real corona discharge device. **Fig. 3 (a)** displays an r–z plane view. The centerline is at the bottom of the analytical model, along the z-axis, which is perpendicular to the r and θ axes. An axisymmetric quasi-two-dimensional analysis is carried out based on cylindrical (r, θ, z) coordinates. The model considered in the numerical method is based on a coaxial needle-to-ring electrode atmospheric NTP reactor. The reactor consists of a needle discharge and a ring-shaped grounded electrode. The needle discharge electrode, which has a negative polarity, is 1 mm in diameter and 4 mm in length. The tip of the needle is spherical. On the ring-shaped grounded electrode, the distance from the origin to the surface of the ring is 5 mm, and the diameter of the cross-section is 1 mm. In the radial direction, the calculation region ranges from r = 0 to r = 9.5 mm. The sharp tip of the high-voltage needle electrode is positioned at r = 0 mm and z = 0 mm, while the surface of the grounded ring electrode is placed at r = 5 mm. It is noted that both the needle and the ring are metal electrodes, and no dielectric barrier exists in the configuration. In the axial z-direction, the calculation region ranges from z = –4 mm to 4 mm. Except for the electrode region, the other boundaries in the model are provided as the outlet or free boundary conditions. Electrons, ions, and radicals, which are induced by the

discharge, flow out of the calculation region. **Fig. 3 (b)** shows a perspective view of the coaxial needle-to-ring electrodes.

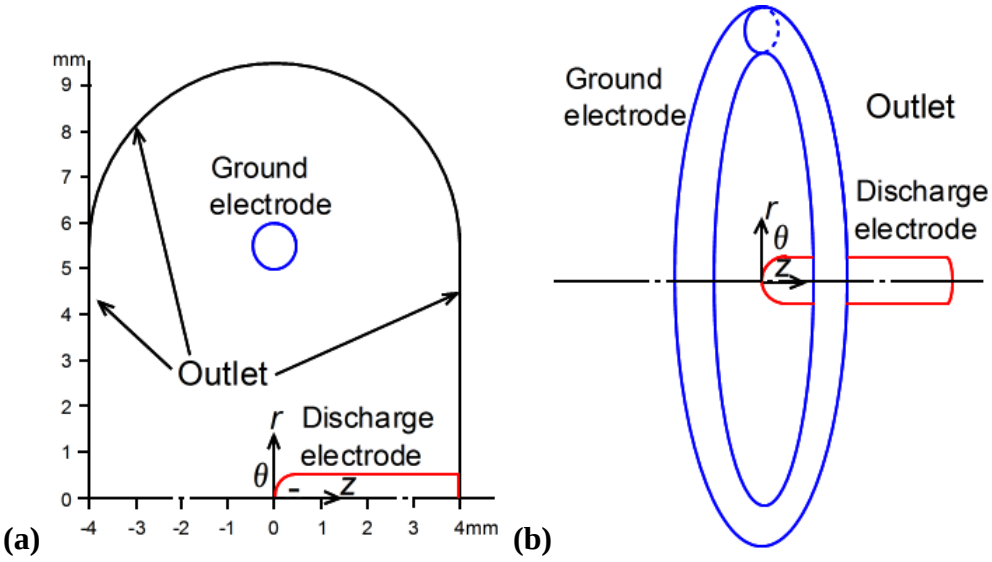

Fig. 3 Analytical model composed of discharge and ground electrodes based on the real corona discharge device. (a) *r*–*z* plane view, and (b) perspective view [4].

Fig. 4 shows the nonuniform computational grid and cells. A three-dimensional (r, θ, z) numerical model is employed, and the gradients of the radial r-direction and the axial z-direction are spatially considered with the assumption that $\partial/\partial\theta = 0$, implying that the model is axisymmetric. The nonstructural analytical mesh used in this study is shown in the figure. The total number of cells is 14,952. The cell used in the study (shown in the figure) is almost uniform. Some trials using fewer cells and a nonuniform mesh model were made before employing the mesh system shown in **Fig. 2**. A satisfactory result could not be obtained in the system with fewer cells.

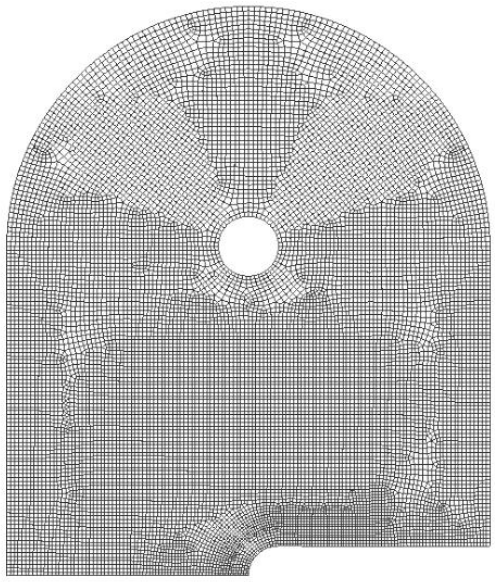

Fig. 4 Computational grids and cells for the numerical calculation (14,952 cells) [4].

3.2.3 Analysis procedure

The following continuum fluid equations [5,6,7] for a two-temperature nonequilibrium NTP are used as the governing equations.

Continuity equation:

$$\frac{\partial \rho}{\partial t} + \nabla \cdot (\rho \boldsymbol{u}) = 0 \tag{1}$$

Momentum equation:

$$\frac{\partial (\rho \boldsymbol{u})}{\partial t} + \nabla \cdot (\rho \boldsymbol{u}\boldsymbol{u}) = -\nabla p + \nabla \cdot (\mu \nabla \boldsymbol{u}) \tag{2}$$

Equation of state:

$$p = \rho R T \tag{3}$$

Energy equation:

$$\frac{\partial (\rho h)}{\partial t} + \nabla \cdot (\rho \boldsymbol{u} h) = \nabla \cdot (\lambda \nabla T) + \psi_{\mathrm{D}} + S_{\mathrm{c}} + n_{\mathrm{e}} \sum_{\mathrm{k}} \varepsilon_{\mathrm{k}} n_{\mathrm{k}} K_{\mathrm{k}} \tag{4}$$

Transport equations of chemical species:

$$\frac{\partial (\rho Y_{\mathrm{i}})}{\partial t} + \nabla \cdot (\rho \boldsymbol{u} Y_{\mathrm{i}}) = \nabla \cdot \boldsymbol{J}_{\mathrm{i}} + M_{\mathrm{i}} \omega_{\mathrm{i}} \tag{5}$$

$$\boldsymbol{J}_{\mathrm{i}} = -\rho D_{\mathrm{i}} \nabla Y_{\mathrm{i}} + \rho Y_{\mathrm{i}} \boldsymbol{u}_{\mathrm{di}} + \boldsymbol{J}_{\mathrm{ci}} \tag{6}$$

$$\omega_{\mathrm{i}} = \sum_{\mathrm{j}=1}^{\mathrm{N_R}} (\nu''_{\mathrm{ij}} - \nu'_{\mathrm{ij}}) q_{\mathrm{j}} \tag{7}$$

$$q_{\mathrm{j}} = k_{\mathrm{j}} \left(\prod_{\mathrm{m}=1}^{\mathrm{N_S}} c_{\mathrm{m}}^{\nu'_{\mathrm{mj}}} - K_{\mathrm{cj}} \prod_{\mathrm{m}=1}^{\mathrm{Ns}} c_{\mathrm{m}}^{\nu''_{\mathrm{mj}}} \right) \tag{8}$$

$$k_{\mathrm{j}} = A_{\mathrm{j}} T_{\mathrm{j}}^{n} \exp(-E_{\mathrm{j}} / RT_{\mathrm{j}}) \tag{9}$$

$$k_{\mathrm{j}} = \int \sqrt{T_{\mathrm{e}}}\, \sigma(T_{\mathrm{e}})\, \mathrm{f}(T_{\mathrm{e}})\, \mathrm{d}\, T_{\mathrm{e}} \tag{10}$$

Electron transport equation:

$$\frac{\partial n_{\mathrm{e}}}{\partial t} + \nabla \cdot \boldsymbol{\Gamma}_{\mathrm{e}} = S_{\mathrm{e}} \tag{11}$$

$$\boldsymbol{\Gamma}_{\mathrm{e}} = \mu_{\mathrm{e}} n_{\mathrm{e}} \nabla \phi - D_{\mathrm{e}} \nabla n_{\mathrm{e}} \tag{12}$$

Electron energy equation:

$$\frac{3}{2} \frac{\partial (n_{\mathrm{e}} T_{\mathrm{e}})}{\partial t} + \nabla \cdot \left(\frac{5}{2} T_{\mathrm{e}} \boldsymbol{\Gamma}_{\mathrm{e}} - \chi \nabla T_{\mathrm{e}} \right) = P_{\mathrm{elec}} - n_{\mathrm{e}} \sum_{\mathrm{k}} n_{\mathrm{k}} K_{\mathrm{k}} \tag{13}$$

Poisson's equation:

$$\nabla \cdot \left(\varepsilon_{\mathrm{r}} \varepsilon_0 \nabla \phi \right) = -\sigma_{\mathrm{c}} \,, \tag{14}$$

where T_{j} (= T_{e} or T) is the absolute temperature of species j. The quantities A_{j}, n, and E_{j} are the constants corresponding to species j, σ is the collision cross-section as a function of T_{e}, and f is the electron energy distribution function (a Maxwell-Boltzmann distribution is assumed). The definitions of the symbols for physical quantities are the same as those stated in our prior publications [5,6].

In our previous studies on atmospheric air plasma [5,6], we considered 197 gas-phase reactions and 21 surface reactions for 25 chemical species, concerning nitrogen and oxygen ions and radicals as well as their excited states. In a previous paper [6], the electron temperature and the abundances of other chemical species calculated with the present plasma model were compared with the experimental data obtained using optical emission spectroscopy. The results

showed the validity of the present plasma model. In the present study, an atmospheric air NTP, including moisture, is tested. The chain of chemical reactions of the positive H_3O^+ ions and the negative O_2^- ions that combine with the moisture in the air to form ion clusters of $H_3O^+(H_2O)_n$ and $O_2^-(H_2O)_n$, respectively, are studied, taking into account the new chemical species. These chain reactions correspond with the reactions based on the chemical reactions reported in the literature [8–14]. Note that n is either a positive integer or zero. For n = 0, although no water molecules are connected to the ions, they are still termed ion clusters in the study. Because of the lack of information on certain details of the chemical reactions, especially the rate constants, the targets are negative and positive ion clusters with n = 0–5. Consequently, 225 gas-phase reactions for 40 chemical species (N, N^+, N_2, N_2^+, $N_2(a^1\Sigma_u^-)$, $N_2(A^3\Sigma_u^+)$, $N_2(B^3\Pi_g)$, $N_2(C^3\Pi_u)$, N_3^+, N_4^+, O, $O(^1D)$, $O(^1S)$, O^+, O^-, O_2, O_2^{**}, $O_2(a^1\Delta)$, $O_2(b^1\Sigma)$, O_2^+, O_2^-, $O_2(v)$, O_3, O_3^-, O_4^+, H_3O^+, H_2O, $H_3O^+(H_2O)$, $H_3O^+(H_2O)_2$, $H_3O^+(H_2O)_3$, $H_3O^+(H_2O)_4$, $H_3O^+(H_2O)_5$, $O_2^-(H_2O)$, $O_2^-(H_2O)_2$, $O_2^-(H_2O)_3$, $O_2^-(H_2O)_4$, $O_2^-(H_2O)_5$, H, OH, and H_2), and 34 surface reactions on the electrodes are considered in a moisture air plasma under atmospheric pressure, based on Refs. [8–14].

A partial set of the reactions of the ion clusters is as follows:

n = 0–4

$$O_2^-(H_2O)_n + H_2O + X \rightarrow O_2^-(H_2O)_{n+1} + X,\ X = O_2,\ k_n \quad (15)$$

m = 1–4

$$O_2^-(H_2O)_{m+1} + X \rightarrow O_2^-(H_2O)_m + X + H_2O,\ X = O_2,\ k_m \quad (16)$$

n = 0–4

$$H_3O^+(H_2O)_n + H_2O + X \rightarrow H_3O^+(H_2O)_{n+1} + x,\ x = O_2,\ X = N_2,\ k'_n \quad (17)$$

m = 0–4

$$H_3O^+(H_2O)_{m+1} + X \rightarrow H_3O^+(H_2O)_m + X + H_2O,\ X = O_2,\ X = N_2,\ k'_m \quad (18)$$

$$e + H_2O \rightarrow e + H + OH\ (E/N = 100\ Td),\ k = 2.0 \times 10^{-9}\ cm^3/s \quad (19)$$

$$H + H_2O \rightarrow H_3O^+ + e\ ,\ (rapid) \quad (20)$$

where k_n, k_m, k'_n, and k'_m are the rate coefficients of cluster formations and are supplied in **Table 1.** It is important to note that the unit of the reaction rate coefficient becomes cm^3/s for two-body reactions and cm^6/s for three-body reactions.

Table 1 Rate coefficients of formation reactions of ion clusters [4].

unit: cm^3/s or cm^6/s	O_2^-		H_3O^+			
	X = O_2		X = O_2 (n = 0–3, m = 1–3) X = Air (n = 4, m = 4)		X = N_2	
m or n	k_n	k_m	k'_n	k'_m	k'_n	k'_m
0	1.6×10^{-28}	–	3.4×10^{-27}	–	3.7×10^{-27}	7.0×10^{-26}
1	5.4×10^{-28}	1.1×10^{-14}	1.85×10^{-27}	1.4×10^{-17}	2.3×10^{-27}	7.0×10^{-18}
2	2.1×10^{-28}	3.0×10^{-13}	1.5×10^{-27}	4.0×10^{-14}	2.4×10^{-27}	3.0×10^{-14}
3	1.0×10^{-28}	1.2×10^{-12}	9.0×10^{-28}	6.0×10^{-12}	–	–
4	5.0×10^{-29}	4.5×10^{-12}	5.0×10^{-31}	2.0×10^{-15}	–	–

Fig. 5 shows the applied pulse voltage waveform of the reactor. The waveform is approximated as a sinusoidal function with a negative peak voltage of –4 kV and a duration time T of 600 ns. These characteristics are the same as those reported in previous studies [5,15]. The use of a pulsed voltage with a very short rise-time (~100 ns) and short duration (1 μs) is considered appropriate for efficient gas cleaning [5,16,17].

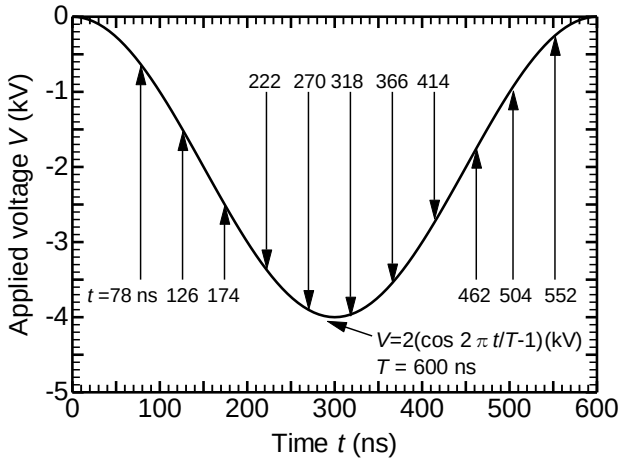

Fig. 5 Waveform of the nanosecond pulse voltage applied at the needle electrode (applied voltage peak = –4 kV, duration time = 600 ns) [4].

The key initial conditions are as follows: gas temperature T = 300 K, p = 100 kPa, electron temperature T_e = 0.2 eV under the quasi-neutrality condition, uniform electron number density $n_e = 8 \times 10^8$ m^{-3}, electric potential $\phi = 0$, and the mass ratios of atmospheric air including water moisture are assumed to be N_2: 76.75 %, O_2: 23.15 %, and H_2O: 0.1 %. It should be noted that calculations with higher moisture could not be successfully executed in the present scheme and should be studied in future studies. The viscosity is calculated using Sutherland's law. The Schmidt and Prandtl numbers are set to 0.7 and 0.707, respectively. The thermal conductivity and specific heat of the stainless steel are set to 16 W/(m K) and 0.5 kJ/(kg K), respectively.

The system of these governing equations is solved simultaneously using the CFD–ACE+ (ESI Group, France) solver [5–7,15]. In this solver, the time-implicit semi-implicit method for the pressure-linked equations-consistent (SIMPLEC) method is used to complete the flow, heat transfer, and chemical analysis using Eqs. (11)–(13). An implicit Poisson solver is used for the electric potential analysis with Eq. (14) under the given boundary conditions. For the unsteady (transient) calculation of the plasma flow, the first-order Euler implicit scheme is adopted. In general, a plasma flow calculation requires a very small time step because the discharge process progresses rapidly. In the current calculation, $\Delta t = 6 \times 10^{-12}$ s = 6 ps is adopted. When Δt exceeds this value, the calculation diverges. The total number of time steps and the full timespan are 100,000 and 600 ns, respectively. The flow and energy fields must be solved with the same time step used in the CFD–ACE+ solver, although the flow and heat parameters are scarcely changed after the 600 ns calculation. In the current simulation, the plasma is only simulated during the first period of the applied voltage because the computation time is fairly long (approximately one month), even with a high-performance PC. It is also noted that grid convergence studies have been carried out. A more divergent grid yields unresolved results. In the future, parallel computing will be attempted to reduce the computing time.

3.2.4 Predicted results for electron number density

Fig. 6 shows the time-dependent electron number density (n_e) distribution obtained from the calculation. A color bar, which indicates the logarithmic value of n_e (in units of m^{-3}), is provided in the figure. Almost no change is observed until a time t = 150 ns has elapsed from the moment when the plasma is turned on. The primary streamer discharge is observed at t = 174 ns, after which the number density gradually increases, starting at the tip of the discharge electrode and extending toward the grounded electrode. The primary streamer proceeds and almost completely crosses the gap between the electrodes. The peak voltage is attained at t = 300 ns, and after t = 318 ns, n_e gradually decreases over the entire region. The value of n_e remains higher near the discharge electrode than in the other regions. It is thought that this is a secondary streamer, followed by the first streamer propagation. The maximum n_e is 4.79×10^{19} m^{-3} at the peak voltage. No obvious streamer head is observed, although it was clearly simulated in our earlier study [5].

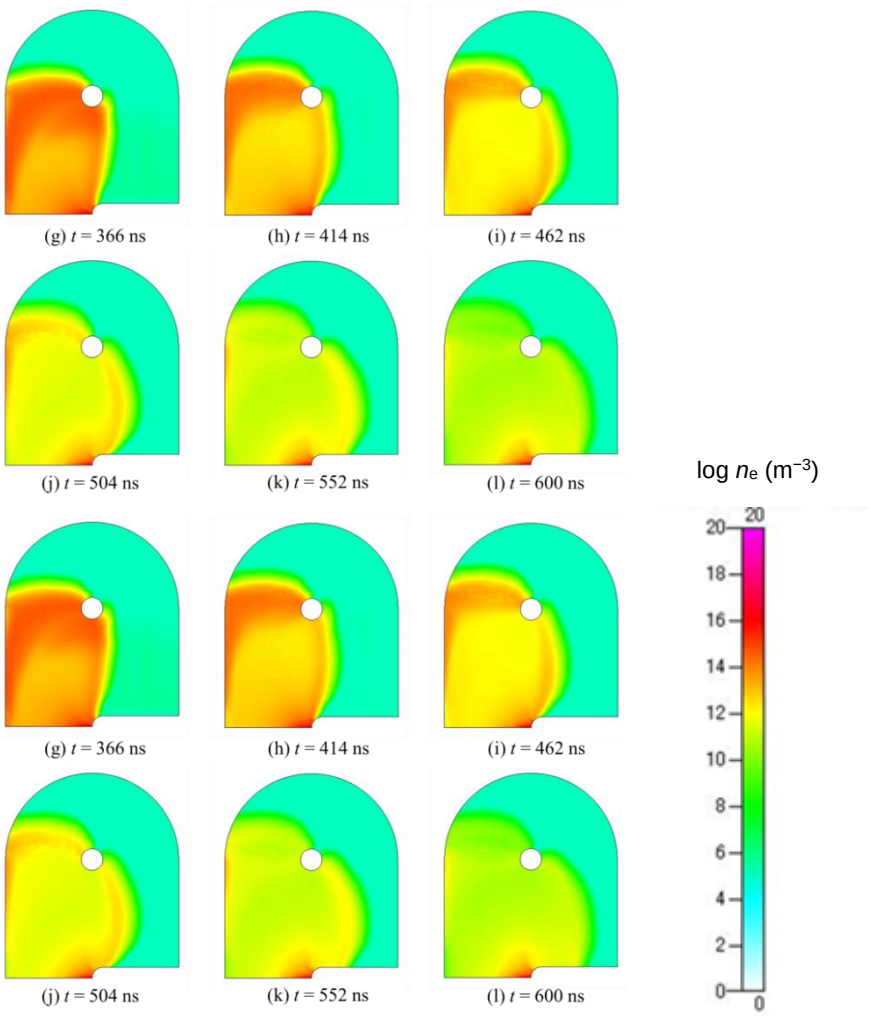

Fig. 6 Result obtained for the time-dependent electron number density (n_e) distribution. The color bar indicates the logarithmic value of n_e [4].

3.2.5 Predicted results for ion cluster number density

Fig. 7 shows the calculated number-density distribution for the time-dependent positive ion cluster $H_3O^+(H_2O)_n$ for $n = 4$. Although it is shown as an example of a calculated result, similar results can also be calculated for $n = 0$, 1, 2, 3, and 5. Almost no change is observed before t = 150 ns from the time the plasma is turned on. However, the number density does increase with an increase in voltage. After t = 174 ns, the density increases gradually, starting at the tip of the discharge electrode and extending toward the grounded electrode. After t = 300 ns, which coincides with the peak voltage, the density remains higher.

Although not all the calculated results are displayed in the figure, it is found that the number densities increase between the discharge gap from the tip to the grounded electrode for all positive ions with n = 0–5. After the peak voltage is attained at t = 300 ns, the number densities of $O_2^-(H_2O)_n$ (n = 3–5) increase slightly. On the other hand, those of $O_2^-(H_2O)_n$ (n = 0–2) decrease. The maximum values of the ion cluster densities for n = 0–5 are as follows: n = 0: 1.10×10^{18} m^{-3}, n = 1: 1.86×10^{18} m^{-3}, n = 2: 1.91×10^{18} m^{-3}, n = 3: 1.70×10^{19} m^{-3}, n = 4: 5.25×10^{19} m^{-3}, n = 5: 7.08×10^{18} m^{-3}.

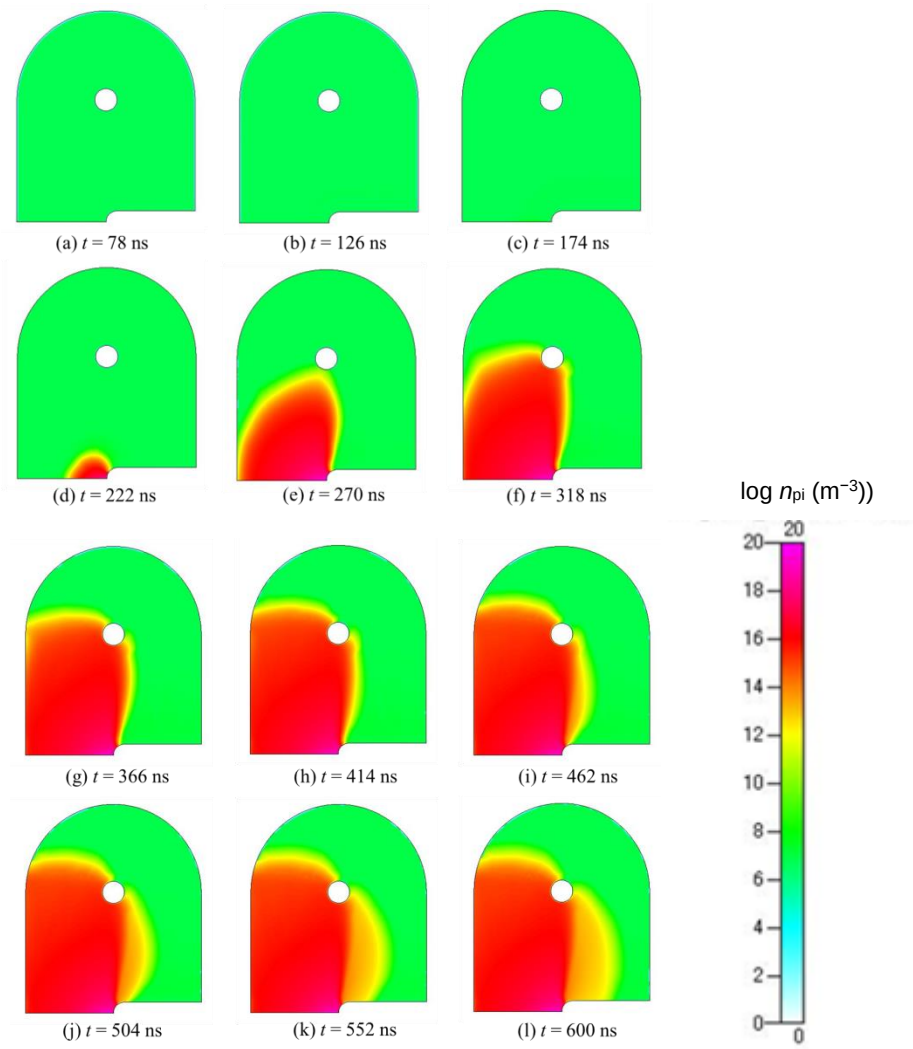

Fig. 7 Result obtained for the time-dependent positive ion cluster $H_3O^+(H_2O)_n$ number-density distribution for n = 4. The color bar indicates the logarithmic value of the ion number density n_{pi} [4].

Fig. 8 shows the calculated number-density distribution for the time-dependent negative ion cluster $(O_2^-(H_2O)_n)$ for n = 4. Although the densities of the negative ion clusters are slightly lower than those of the positive ion clusters, the qualitative behaviors for negative n = 0–5 ion clusters are almost the same as those for positive n = 0–5 ion clusters. The maximum values of the ion cluster densities for n = 0–5 are as follows: $n = 0 : 4.27 \times 10^{18}$ m^{-3}, $n = 1 : 1.10 \times 10^{18}$ m^{-3}, $n = 2 : 2.04 \times 10^{18}$ m^{-3}, $n = 3 : 2.27 \times 10^{18}$ m^{-3}, $n = 4 : 4.27 \times 10^{18}$ m^{-3}, $n = 5 : 1.74 \times 10^{18}$ m^{-3}.

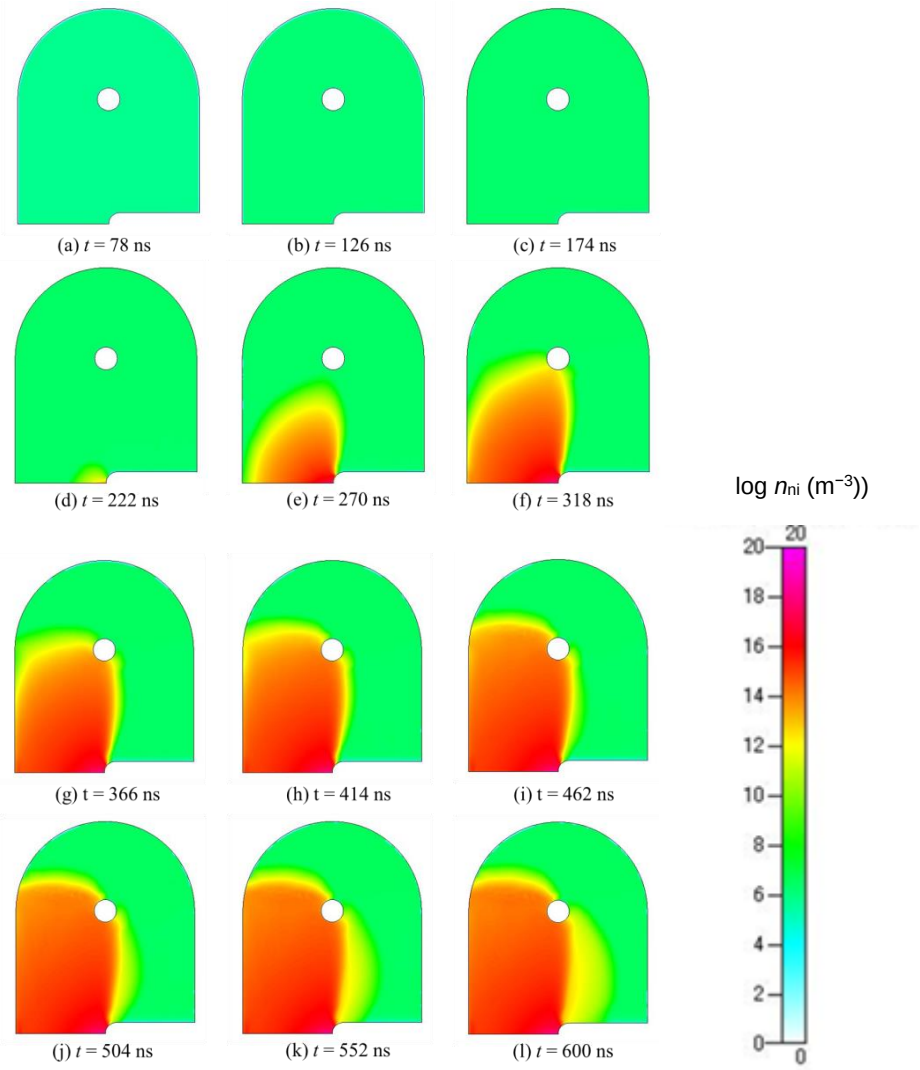

Fig. 8 Result obtained for the time-dependent negative ion cluster ($O_2^-(H_2O)_n$) number-density distribution for n = 4. The color bar indicates the logarithmic value of the ion number density n_{ni} [4].

3.2.6 Predicted results for the total generation of ion clusters

Fig. 9 (a) shows the time-dependent total number of positive ion clusters generated by a pair of needle-to-ring electrodes, for six types of clusters. In this figure, the horizontal axis is assumed to represent elapsed time, and the vertical axis represents the number of ions generated, the unit of which is the molecule. As seen in the graph, all the types of ion clusters begin to be generated at approximately 150 ns. At the peak voltage coinciding with t = 300 ns, the number of clusters with n = 0–5 has increased significantly. After this peak, clusters with n = 0–2 decrease in number, clusters with n = 3 stay constant, and clusters with n = 4 and 5 increase in number. It is concluded that positive ion clustering progresses over time. At the end of the pulse, the generation of $H_3O^+(H_2O)_4$ (n = 4) is at its highest: 5.17×10^9 #, where # means the number. The differing generation numbers for the respective types of ion clusters are due to the differences in the rate coefficients of the chemical reactions forming the clusters, as shown in **Table 1**.

Fig. 9 (b) shows the time-dependent total number of negative ion clusters generated by a pair of needle-to-ring electrodes for six types of clusters. It is evident that the graph exhibits a similar qualitative tendency to that in **Fig. 9 (a)**. The clustering of negative ions progresses over time. At the end of the pulse, all the counts of the generated negative ion clusters tend to be constant. The number of $O_2^-(H_2O)_4$ (n = 4) ions generated is the highest at 4.25 ×10^8 #.

We conclude that the clustering processes for both the negative and positive ions have been successfully simulated in the current numerical simulation. Approximately a total of 10^5 cm^{-3} of negative and positive ions are generated with a single ion-generated device. In the next section, the results of the application of the NTP air cleaner to an actual plant factory are described. It is noted that the positive and negative ion clusters ($n > 0$) targeted in the current study have a relatively long lifetime compared to the O_2^- and H_3^+ radicals themselves. The cleansing effect of air decomposes viruses, hazardous materials, and air pollutants suspended in the atmosphere when ion clusters are discharged into the air [3,4]. The positive and negative ion clusters bond to the surfaces of airborne viruses and other substances and change into OH radicals [3,4], which have cleansing effects. Therefore, it is important to find the plasma condition that yields the optimum number of ion clusters to achieve the optimal design goals of the electrode systems.

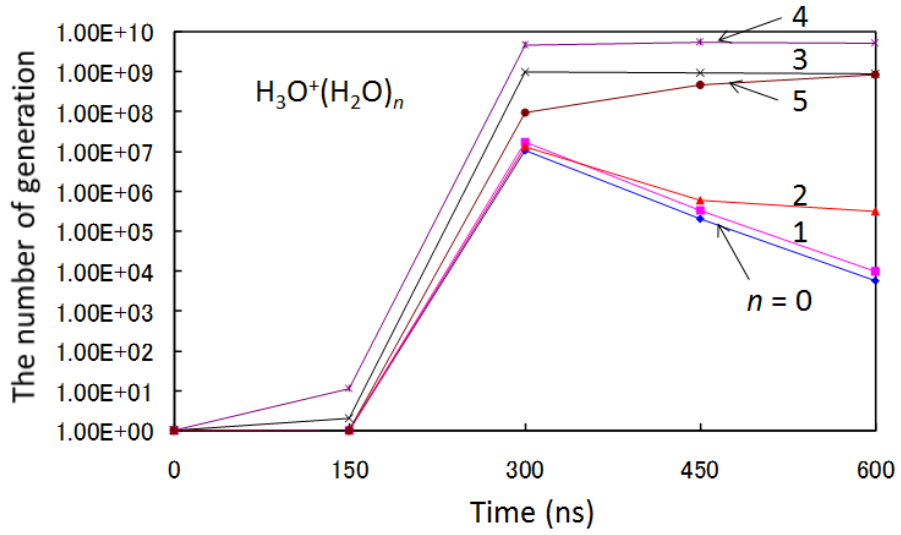

(a)

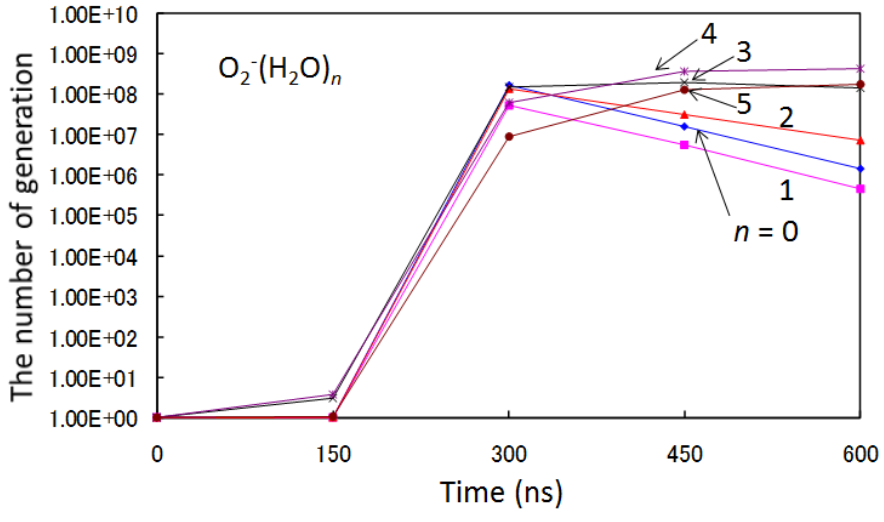

(b)

Fig. 9 Results obtained for the time-dependent total number of ion clusters generated by a pair of needle-to-ring electrodes. The horizontal axis represents elapsed time and the vertical axis represents the number of ions generated, the unit of which is the molecule. (a) Positive ion clusters $H_3O^+(H_2O)_n$ (n = 0–5) and (b) negative ion clusters $O_2^-(H_2O)_n$ (n = 0–5) [4].

4. Application of a nonthermal plasma air cleaner

4.1 Introduction of the air cleaner to cleanroom for plant factory

In addition to the numerical simulation, we test a plasma air cleaner to determine its effect in a cleanroom in a plant factory. Originally, an air cleaner with a HEPA filter was installed in the cleanroom. However, HEPA filters are expensive and induce a large pressure loss. In addition to experimentally validating the numerical simulation, we propose a low-cost plasma air cleaner as an alternative to expensive HEPA filters. Therefore, in this study, the plasma air cleaner is operated in a cleanroom with and without the HEPA filter in operation to investigate the sterilization effect, particularly for airborne bacteria.

The top view of the cleanroom at Osaka Prefecture University, C21 building for measuring airborne bacteria is shown in **Fig. 10**. The photograph is shown in **Fig. 11**. The positions of the two HEPA filters are indicated in **Fig. 10**. PCI is used as an acronym for "plasma cluster ion" devices; the positions of these devices are also indicated in **Fig. 10**. PCI1 is a floor-standing-type plasma air cleaner, and the four PCI2 units are ceiling-mounted plasma air cleaners. The external dimensions of PCI1 are 392 mm in width × 182 mm in depth × 500 mm in height, and the flow rate is 4.5 m^3 min^{-1}. The dimensions of the exit of the PCI2 units at the ceiling are 281 mm × 170 mm. A flow rate of 0.58 m^3 min^{-1} is used.

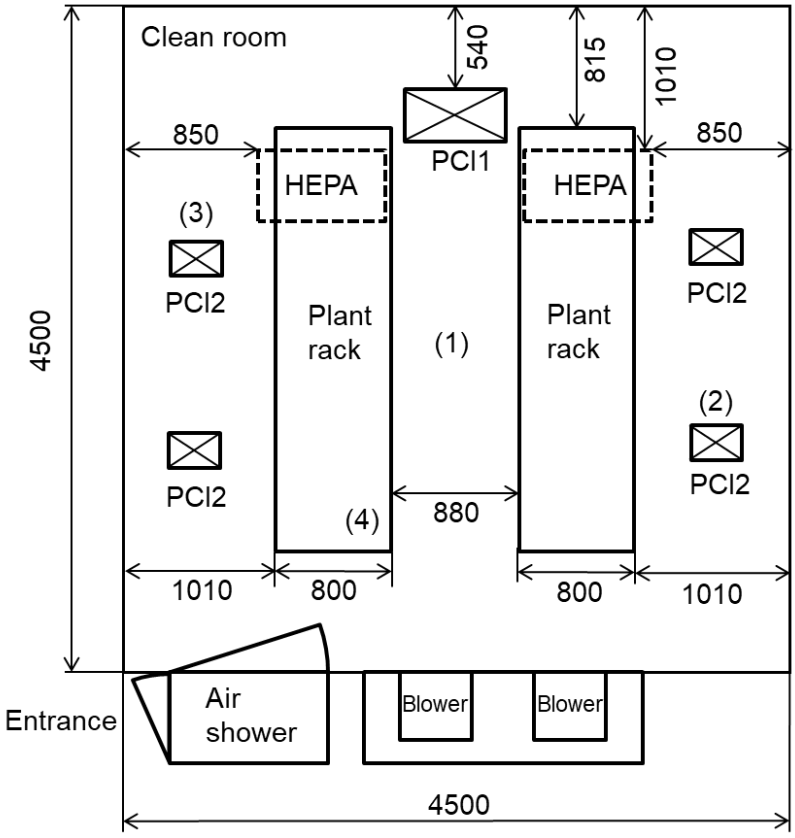

Fig. 10 Overview of the cleanroom for the plant factory.

(a)

(b)

Fig. 11 Photograph of the cleanroom for the plant factory.

In addition, there are two plant racks (total height 222 mm) shown on the left and right of **Fig. 10** in the cleanroom, and iceplants are planted on both of them, as shown in **Fig. 11**. Each rack is divided into three shelves: lower, middle, and upper. The plants are planted in the lower and middle tiers. The positions where the airborne bacteria and ion concentration are measured are shown by (1)–(4) in **Fig. 10**. Position (1) indicates the central part of the cleanroom, (2) is near the PCI2 in the lower right of the figure, (3) is near the PCI2 in the upper left of the figure, and (4) is the position in the left plant rack. In addition, positions (1) to (3) are located at a height of 1 m from the floor surface, and position (4) is determined by placing a measuring instrument in the middle shelf of the left plant rack. For the ion concentration, the spatial concentration of positive and negative ions is measured using a spatial ion concentration meter.

4.2 Measurement condition and apparatus for suspended bacteria and true fungi

Four experiments were conducted; two experiments each for two types of airborne bacteria. The types of bacteria are general bacteria such as *Staphylococcus aureus*, and true fungi. Each type was measured with the HEPA filters on and off, respectively. Sampling was performed with two devices, two times each day for total six days. At each day, a period of one week was

taken. The plasma air cleaner was switched on for the first, third, and fifth days, and it was switched off for the second, fourth, and sixth days.

In these experiments, two devices were used to measure airborne bacteria. The first was the MBS-1000D (Midori Anzen Co., ltd.) airborne bacterium measuring instrument. Air was sucked into the measuring instrument from its upper part, and the sucked air was blown onto the surface of the agar medium in the measuring instrument to collect airborne bacteria. The sampling flow rate was 100 L min^{-1}. Measurements was made for 5 min, and the sampling volume was 500 L. The second device used to measure airborne bacteria was the RCS air sampler (Merck KGaA). The wing of the device rotated and blowed air onto the surface of the medium to collect airborne bacteria. The sampling flow rate was 40 L min^{-1}. The measurement was performed for 8 min, and the sampling volume was 320 L. The measurement result was converted to a sampling volume of 500 L. The culture medium for each sample is shown below.

For bacteria (*Staphylococcus aureus*, etc.), standard agar medium (Nihon Pharmaceutical Co., Ltd.), and Agar Strip TC (total count) (Biotest Co., Ltd.) was used. For true fungi, potato dextrose agar with chloramphenicol (Kohjin Bio Co., Ltd.) and Agar Strip YM (yeasts and molds) (Biotest Co., Ltd.) was used. Bacteria and fungi were measured twice each, with two types of devices at each of the locations (1)–(4), as shown in **Fig. 10**. The measurements were performed for six days. The medium was cultured at a constant temperature for a certain period of time. The method is as follows: Bacterial medium was incubated for 72 h at a temperature of 35 °C. Similarly, the fungal medium was cultured for 120 h at 25°C.

4.3 Results and discussion

4.3.1 Results for bacteria

Fig. 12 shows the measurement results of the relationship between the average ion concentration and the average number of bacteria with the HEPA filters switched on. The horizontal axis represents the average concentration of negative and positive ions at each measurement point, the vertical axis represents the average number of microorganisms in 500 L of air detected with the two types of measuring devices, and the error bar indicates the standard deviation $\pm\sigma$. The same descriptors apply to **Figs. 13–15**, except that the measurements shown in **Fig. 13** and **Fig. 15** are taken with the HEPA filters off. The measurements indicate that the average number of bacteria is small and that the number of bacteria does not depend on the ion concentration. No effect due to the plasma air cleaner is observed.

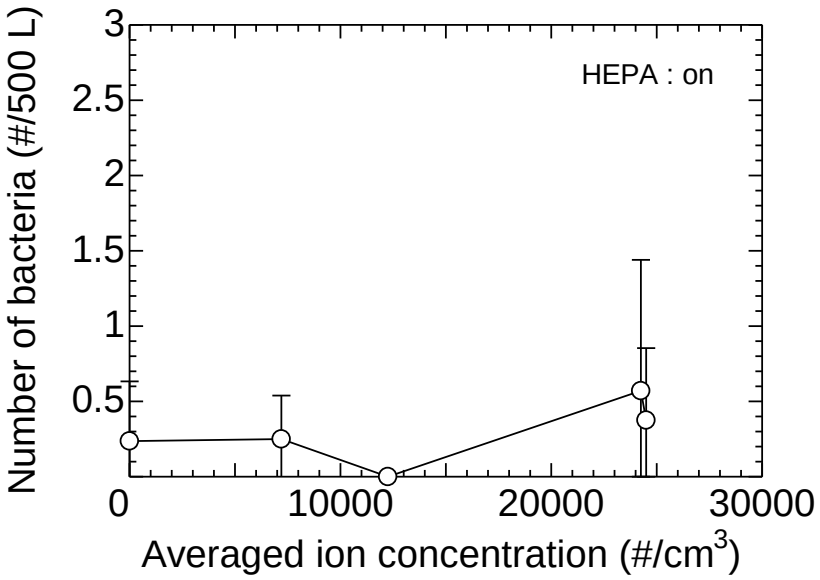

Fig. 12 The measured relationship between the average number of ions and the number of bacteria (HEPA: on)

Fig. 13 shows the measurement results of the relationship between the average ion concentration and the average number of bacteria with the HEPA filters off. The measurements indicate that the average number of bacteria is relatively large (because the HEPA filters are not used), and the measurement data fluctuate greatly. However, the number of bacteria could show no dependence on the ion concentration, and no effect of the plasma air cleaner is observed.

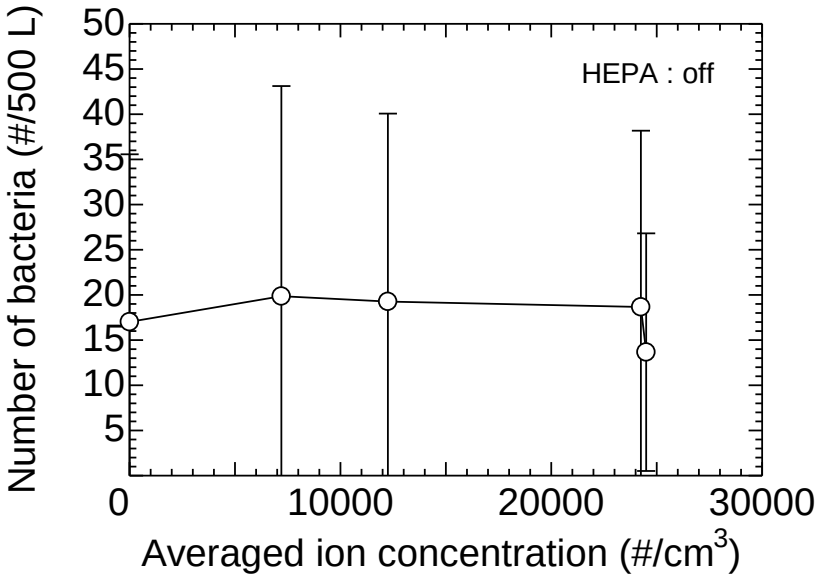

Fig. 13 The measured relationship between the average number of ions and the number of bacteria (HEPA: off)

4.3.2 Results for true fungi

Fig. 14 shows the measurement results of the relationship between the average ion concentration and the average number of fungi with the HEPA filters switched on. The measurements indicate that the average number of fungi is small (because the HEPA filters are used), and the measurement data fluctuate greatly. However, the number of fungi decreases with an increase in ion concentration. When an ion air cleaner is used in combination with HEPA filters, the maximum removal efficiency of true fungi is 99.7%.

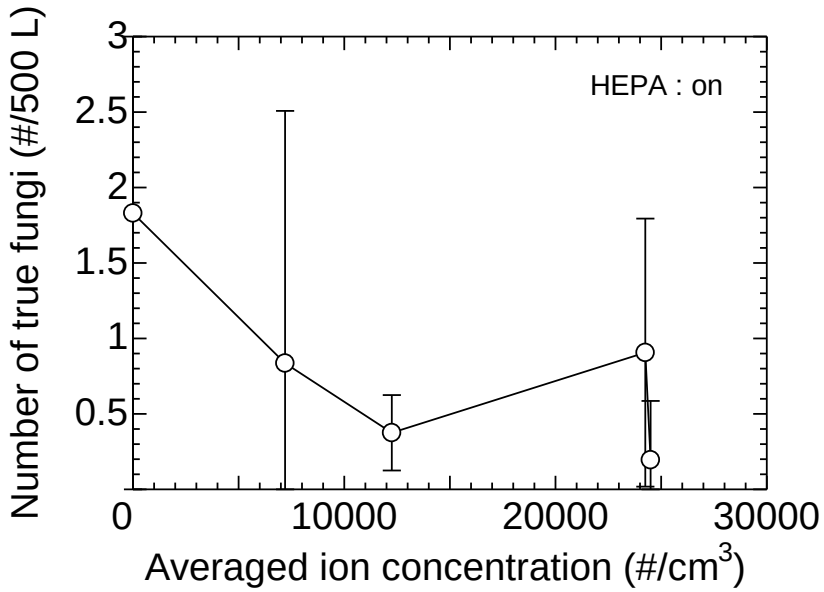

Fig. 14 The measured relationship between the average number of ions and the number of true fungi with HEPA filters on.

Fig. 15 shows the measurement results of the relationship between the average ion concentration and the average number of true fungi with the HEPA filters off. As shown in the figure, the average number of fungi is relatively large (because the HEPA filters are not used), and the measurement data fluctuate greatly. However, the number of true fungi decreases with an increase in ion concentration. When only the ion air cleaner is used, the maximum removal efficiency of true fungi is 91.8%.

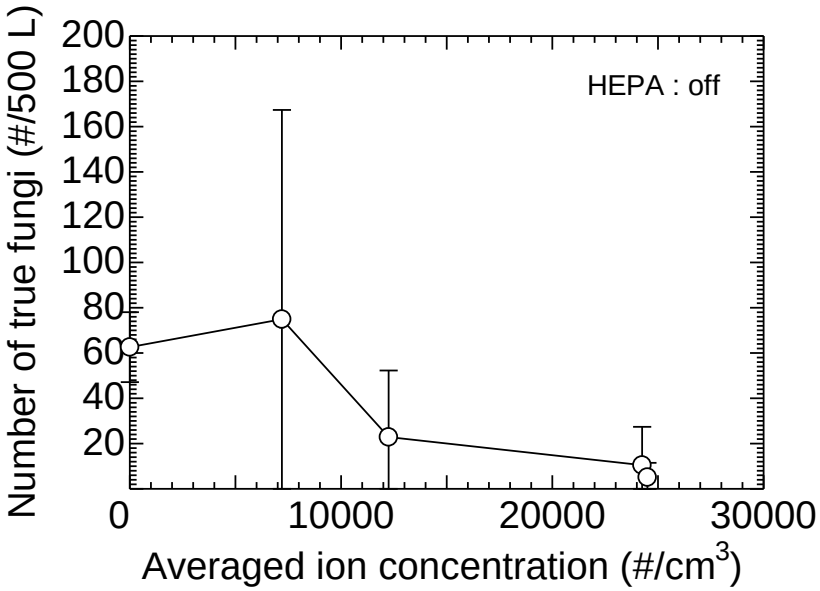

Fig. 15 The measured relationship between the average number of ions and the number of true fungi with HEPA filters off.

5. Conclusions

This study demonstrates that the low pressure-loss plasma air cleaner could replace a HEPA air cleaner. Numerical and experimental studies of pulsed, high-voltage-induced ion cluster formations are carried out. The findings of the current study are useful for the design of ion generator type of indoor air cleaners. The ion generation parts of the air cleaner can be designed with a numerical simulation. Furthermore, the measurements of the average number of airborne bacteria in the cleanroom of the plant factory do not demonstrate the effect of the plasma cluster on bacteria. The measurements of the average number of true fungi in the cleanroom of the plant factory demonstrate that the plasma cluster is effective for true fungi. When an ion air cleaner is used in combination with HEPA filters, the maximum removal efficiency of true fungi is 99.7%. When the ion air cleaner is used solely, the maximum removal efficiency of true fungi is approximately 91.8%.

Acknowledgment

The author would like to thank Mr. K. Kanayama and Mr. Y. Hiroyasu (former graduate students at Osaka Prefecture University) for conducting the numerical simulations and experiments. The present text is a review of their authored thesis [1] and papers [4].

Reference

[1] D. Kanayama, “2D Numerical simulation considering ion cluster chemical reactions,” Master’s Thesis, Department of Mechanical Engineering at Osaka Prefecture University, 2014 (in Japanese).

[2] S. Maruyama, “Control of culture environment and cleaning techniques for closed plant factory,” *Earozoru Kenkyu*, **31**, pp. 104–109, 2016 (in Japanese) doi:10.11203/jar.31.104

[3] Sharp Corporation website, 2020. [Online]. Available: https://global.sharp/pci/en/about_pci/

[4] M. Okubo, Y. Hiroyasu, and T. Kuroki, Ion Cluster Formation by Nonthermal Plasma Induced by Pulse Corona Discharge Toward Indoor Air Cleaning, *IEEE Trans. Ind. Applicat*., vol. 56, no. 5, pp. 5480–5488, 2020.
[5] M. Okubo, "Evolution of streamer groups in nonthermal plasma," Physics of Plasmas, vol.22, no. 12, 123515, 2015.
[6] M. Okubo, K. Yoshida, and T. Yamamoto, "Numerical and experimental analysis of nanosecond pulse dielectric barrier discharge-induced nonthermal plasma for pollution control," *IEEE Trans. Ind. Appl*., vol. 44, 1410, 2008.
[7] T. Kuroki, S. Tanaka, M. Okubo, and T. Yamamoto, "Numerical investigation for CF_4 decomposition using RF low pressure plasma," *IEEE Trans. Ind. Applicat*., vol. 43, no. 4, pp. 1075–1083, 2007.
[8] K. Nagato, Y. Matsui, T. Miyata, and T. Yamauchi, "An analysis of the evolution of negative ions produced by a corona ionizer in air," *Int. J. Mass Spectrometry*, vol. 248, pp. 142–147, 2006.
[9] M. L. Huertas, J. Fontan, and J. Gonzalez, "Evolution times of tropospheric negative ions," *Atmospheric Environment*, vol. 12, pp. 2351–2362, 1978.
[10] K. Ikebe, K. Nakanishi, and S. Arai, "Evolution process of microdischarge products in ozonizer," *Trans. IEE Japan*, vol. 109-A, 11, pp. 474–480, 1989 (in Japanese).
[11] R. Dorai, "Modeling of plasma remdediation of NO_x using global kinetic models accounting for hydrocarbons," Ph.D. Thesis, Univ. Illinois at Urbana-Champaign, 2000.
[12] J. C. Person, J. C. Personm, and D. O. Ham, "Removal of SO_2 and NO_x from stack gases by electron beam irradiation," *Radiat. Phys. Chem*. vol. 31, nos. 1–3, pp. 1–8, 1988.
[13] T. E. Parts and A. Luts, "Observed and simulated effects of certain pollutants on small air ion spectra: I. positive ions," *Atmospheric Environment*, vol. 38, issue 9, pp. 1283–1289, 2004.
[14] M. L. Huertas and J. Fontan, "Evolution times of tropospheric positive ions," *Atmospheric Environment*, vol.12, pp. 1018–1026, 1975.
[15] T. Sato, D. Ito, and H. Nishiyama, "Reactive flow analysis of nonthermal plasma in a cylindrical reactor," *IEEE Trans. Ind. Appl*., vol. 41, no. 4, pp. 900–905, Jul./Aug. 2005.
[16] T. Matsumoto, D. Wang, T. Namihira, and H. Akiyama, "Energy efficiency improvement of nitric oxide treatment using nanosecond pulsed discharge," *IEEE Trans. Plasma Sci*., 38, 2639, 2010.
[17] D. Wang, T. Matsumoto, T. Namihira, and H. Akiyama, "Development of higher yield ozonizer based on nano-seconds pulsed discharge," *J. Adv. Oxid. Technol*., 13, 71, 2010.